Nano Research

Open Access

Research Article

Weakly solvating electrolyte enabling solvent-free co-intercalation for stable potassium-ion storage in graphite

Chaojie Cheng[1], Wencong Feng[1], Feiyue Wang[1], Jingke Ren[1], Deyang Guan[2], Wei Chen[1], Jean-Jacques Gaumet[1,3], Kai Fu[1]✉, Xiaobin Liao[1]✉, and Wen Luo[1]✉

[1] *State Key Laboratory of Advanced Technology for Materials Synthesis and Processing, School of Materials Science and Engineering, Wuhan University of Technology, Wuhan 430070, China*
[2] *School of Materials Science and Engineering, Xinjiang University, Urumqi 830017, China*
[3] *Laboratoire de Chimie et Physique: Approche Multi-échelles, des Milieux Complexes (LCP-A2MC), Institut Jean Barriol, Université de Lorraine, Metz 57070, France*

Cite this article: *Nano Research*, **2025**, *18*, 94907219. https://doi.org/10.26599/NR.2025.94907219

ABSTRACT: Ether electrolytes for potassium-ion batteries exhibit a broader electrochemical window and greater applicability, yet most of them are high-concentration electrolytes with elevated cost. In this study, we propose the use of a weakly solvating cyclic ether electrolyte with tetrahydropyran (THP) as the solvent. This approach induces the formation of a thin and dense inorganic-rich solid electrolyte interphase (SEI) film, which is accompanied by a decrease in the activation energy of electrode interfacial reactions due to the weak ligand binding of THP with K^+. Density functional theory (DFT) simulations also corroborate the hypothesis that K^+ has a lower binding energy with THP. During potassium storage process, the phenomenon of solvent co-intercalation of graphite does not occur, which greatly reduces the destruction of the graphite structure and enables a superior electrochemical performance and enhanced cycling stability at a lower concentration (2 M). At a current density of 0.2 C (55.8 mA·g^{-1}), the battery can be stably cycled for 800 cycles (approximately 8 months) with a specific capacity of 171.8 mAh·g^{-1}. This study provides a new ether-based electrolyte for potassium ion batteries and effectively reduces the electrolyte cost, which is expected to inspire further development of energy storage batteries.

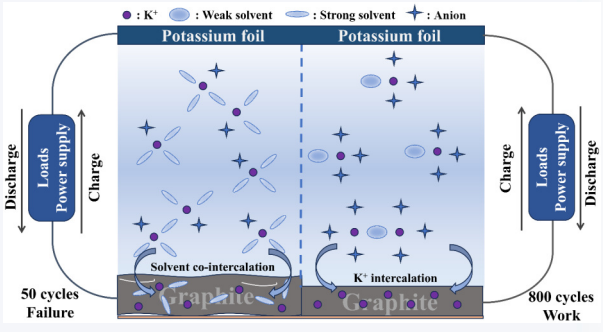

KEYWORDS: weakly solvating electrolyte, co-intercalation, graphite, potassium ion batteries

1 Introduction

The advancement of technology has stimulated a marked increase in energy consumption, resulting in inadequate power supply during peak periods and surplus power during low-peak periods [1]. It is therefore evident that there is a requirement for the construction of low-cost, large-scale energy storage system in order to meet the energy needs of modern society. Potassium ion batteries are regarded as a highly promising energy storage unit for the construction of large-scale energy storage system [2, 3], primarily due to the inexpensive and plentiful availability of potassium resources and the fact that potassium ions possess a relatively low standard electrode potential of –2.93 V vs. standard hydrogen electrode (SHE) [4–6]. Moreover, potassium ions can be incorporated into graphite to form KC_8 compounds analogous to lithium ions, with a theoretical specific capacity of 279 mAh·g^{-1} [7–9]. Despite the development of numerous anode materials (including carbon materials [3, 10–13], alloy materials [14–19], and transition metal sulfides [20–23]), graphite remains the most promising anode material for potassium ion batteries. Its advantages include a low voltage plateau, cost-effectiveness, and environmental compatibility. Electrolytes are a critical component in enabling stable cycling in batteries. To fully utilize the potential of graphite anodes, it is essential to optimize the electrolyte composition to align with the unique properties of this anode material.

The traditional electrolyte, composed of carbonate as the solvent and potassium hexafluorophosphate (KPF_6) as the solute, begins to decompose at 4 V and above, resulting in the formation of a solid

Received: November 14, 2024; **Revised:** December 20, 2024
Accepted: December 25, 2024

✉Address correspondence to Wen Luo, luowen_1991@whut.edu.cn; Kai Fu, kaifu@whut.edu.cn; Xiaobin Liao, xiaobinliao@whut.edu.cn

electrolyte interphase (SEI) film rich in organic components at the anode [24]. This film is unable to promote the long-term stable cycle of the battery. In contrast, ether solvents possess a wider electrochemical window and greater applicability due to their higher highest occupied molecular orbital (HOMO) and lowest unoccupied molecular orbital (LUMO) energies. The most used ether-based electrolyte solvents are ethylene glycol dimethyl ether (DME), diethylene glycol dimethyl ether (DEGDME), and tetraethylene glycol dimethyl ether (TEGDME). However, at lower concentration (< 3 M), co-intercalation of solvent molecules and potassium ions into the graphite layers would cause interlayer peeling of graphite [25], therefore resulting in a low reversibility capacity. Additionally, this co-intercalation leads to an increase in the voltage platform, which would result in a decrease in the output voltage and energy density of the full battery. Generally, a concentration of electrolyte exceeding 5 M can prevent the embedding of solvent molecules into the graphite interlayer with potassium ions, thereby reducing the voltage plateau [24]. Nevertheless, the high concentration of electrolyte will result in a considerable increase in cost.

Therefore, based on the mechanism of high-concentration electrolytes, we have chosen tetrahydrofuran (THF) and tetrahydropyran (THP) as the solvent, two cyclic ethers with relatively large ring structures. By utilizing their weak solvating abilities, we aim to reduce the coordination between solvent molecules and potassium ions in solvated potassium ions, thereby enabling solvent-free potassium ion intercalation into graphite at lower concentrations. Furthermore, through molecular dynamics (MD) simulations of the solvation structure of potassium ions, their weakly solvated nature has been verified. Density functional theory (DFT) calculations reveal that potassium ions have the lowest binding energy with THP, making it easier for them to undergo desolvation. This approach demonstrates to enhance the capacity and cycling stability of potassium-ion batteries with graphite anodes in electrolytes with lower concentration.

2 Results and discussion

Since DME is commonly used as an electrolyte solvent, it is selected as a representative of solvents with strong solvating abilities as a contrast. DME is a chain ether with a donor number of up to 20 and a moderate dielectric constant of approximately 7.2 at room temperature (25 °C) [24], which contributes to its high Lewis basicity and solubility for electrolyte salts. THP and THF have donor numbers of 22 and 20, respectively, and dielectric constants of 5.5 and 7.4 [26]. These properties make THP, THF, and DME comparable in terms of their solvent characteristics, ensuring adequate solubility for electrolyte salts. However, the cyclic structures of THP and THF introduce greater steric hindrance, which would affect the actual solubility of potassium salts and their solvated structures. For all three kinds of electrolytes, potassium bis(fluorosulfonyl)imide (KFSI) was chosen as the electrolyte salt, with a concentration of 2 M (denoted as 2 M KFSI in solvent). The linear sweep voltammetry curves for three kinds of electrolytes are shown in Fig. S1 in the Electronic Supplementary Material (ESM). The decomposition voltages of the THP-based, THF-based, and DME-based electrolytes are 4.8, 4.4, and 3.5 V, respectively. The solvated structures of the three electrolytes were investigated by using infrared (IR) spectroscopy and Raman spectroscopy. In the IR spectra (Fig. 1(a)), the FSI^- peak is located at 1174.4 cm^{-1}. In

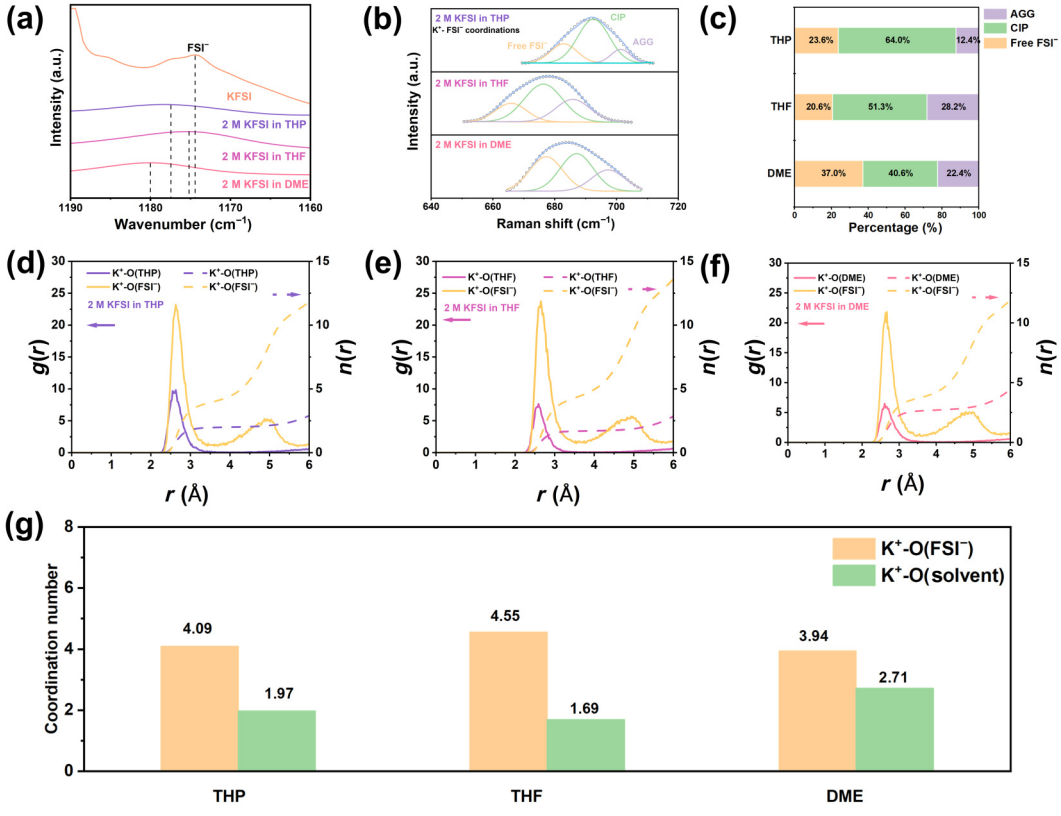

Figure 1 (a) Infrared spectra of electrolyte and solute salt. (b) Raman spectra of the electrolyte. (c) Coordination fitting results of FSI^-. (d)–(f) Radial distribution function (solid line) and coordination number (dashed line) calculated based on O sites surrounding K^+ in the electrolyte. (g) Comparison of coordination numbers among different electrolytes.

2 M KFSI in DME, THF, and THP, the FSI^- peak shifts to 1179.7, 1177.3, and 1175.4 cm^{-1}, respectively. These shifts indicate that the degree of K^+-FSI^- coordination increases in the order of DME < THP < THF. In the Raman spectrum (Fig. 1(b)), based on the degree of coordination between K^+ and FSI^-, the spectral peaks can be divided into three parts: free FSI^-, contact ion pairs, and aggregates [27]. By fitting the proportions, the percentages of various coordination entities of K^+ and FSI^- in the solvated structures were calculated (Fig. 1(c)). The results show that the degree of K^+-FSI^- coordination increases in the order of DME < THP < THF in the three electrolytes. Therefore, K^+ in 2 M KFSI in THF has more coordination with FSI^- than in THP and DME. FSI^- is deeply involved in the solvated structure of K^+, confirming the order of solvating abilities of the three solvents as THF < THP < DME.

To further investigate the solvated structures, MD simulations on the three kinds of electrolytes were conducted [28], using the model presented in Fig. S2 in the ESM. In the radial distribution functions (RDFs) of oxygen atom sites surrounding K^+ (Figs. 1(d)–1(f)), the two peaks located at approximately 2.5 Å from K^+ correspond to K^+-O(FSI^-) pairs and K^+-O(solvent) pairs, respectively. The coordination numbers (n) of K^+ with O sites in the three kinds of electrolytes were calculated using the Eq. (1) and are presented in Fig. 1(g)

$$n(r') = 4\pi\rho\int_0^{r'} g(r)\, r^2 \mathrm{d}r \quad (1)$$

where, $g(r)$ represents the radial distribution function; ρ denotes the number density, which is N/V.

The coordination numbers for the three kinds of electrolytes indicate that in THF, the K^+-O(solvent) interaction is the weakest, while the K^+-O(FSI^-) interaction is the strongest. This aligns with the previous IR and Raman spectroscopy tests. The simulated coordination numbers of K^+-O(FSI^-) are THF (4.55) > THP (4.09) > DME (3.94). This once again verifies that the solvation ability increases in the order of THF < THP < DME.

Furthermore, to gain a deeper understanding of the fundamental properties of the three kinds of electrolytes, THF, THP, and DME, DFT calculations were conducted. The calculated HOMO and LUMO energies for THF, THP, and DME are relatively similar (Fig. 2(a)), indicating that these three kinds of ethers possess comparable decomposition potentials and similar stability. The electrostatic potential distributions of the three kinds of solvent molecules are shown in Fig. 2(b), revealing that the O atoms in the ether bonds have the strongest electronegativity and are more prone to strong interactions with K^+. Moreover, the electronegativity of the O atoms in the ether bonds increases in the order of O_{DME} < O_{THP} < O_{THF}. When these O atoms coordinate with K^+, solvents with stronger electronegativity will be closer to the potassium ions due to electrostatic forces. When the solvent molecules are of similar size, fewer coordination sites will be available, resulting in a decrease in their coordination numbers. This may also be one of the reasons why THF has a higher dielectric constant than THP but a lower coordination number for K^+-O solvent. Additionally, we calculated the binding energies for the coordination of THF, THP, and DME with K^+ (Fig. 2(c)), which are ΔE_{THF} (–0.97 eV) > ΔE_{THP} (–0.94 eV) > ΔE_{DME} (–0.82 eV). Considering that two O atoms in the DME molecule can simultaneously participate in coordination, the binding energy would be even higher. A higher binding energy between K^+ and solvent leads to a slower desolvation process and may even result in solvent co-intercalation into graphite. The IR spectra of the three

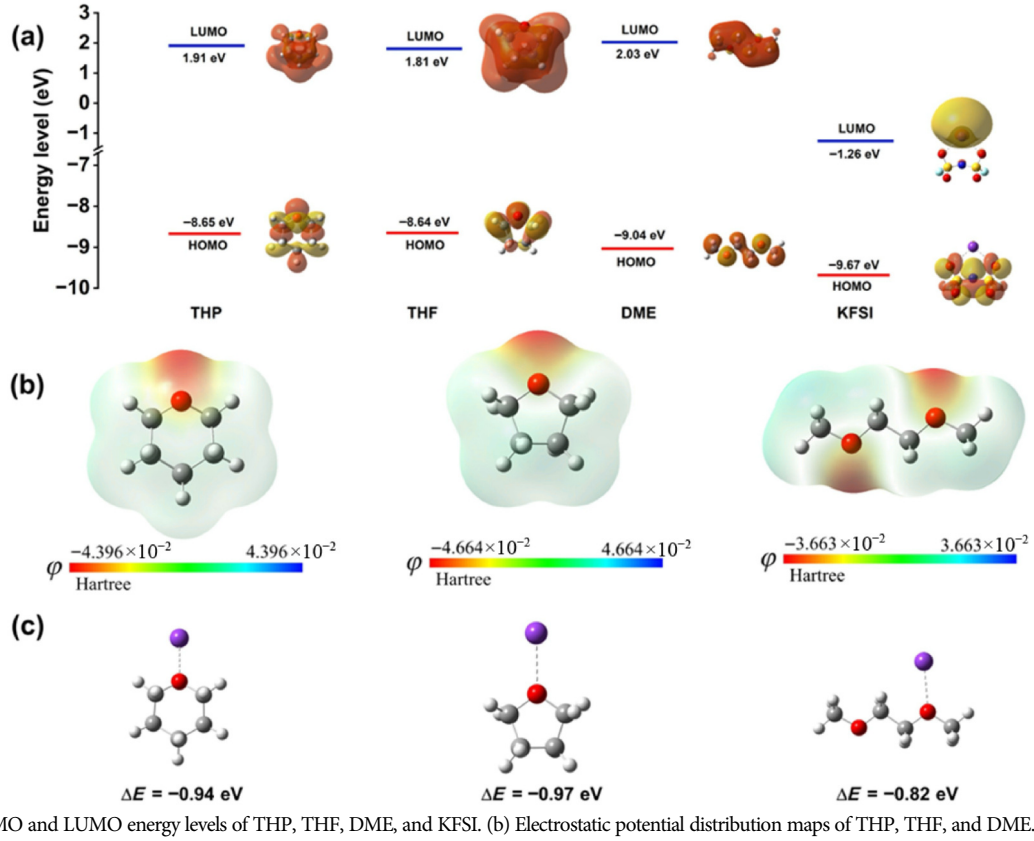

Figure 2 (a) HOMO and LUMO energy levels of THP, THF, DME, and KFSI. (b) Electrostatic potential distribution maps of THP, THF, and DME. (c) Binding energy of K^+ with THP, THF, and DME.

kinds of electrolytes are shown in Fig. S3 in the ESM. Upon adding potassium salt, the ether bond in THP shifts by 5.8 cm^{-1}, THF by 12.5 cm^{-1}, and DME by 17.8 cm^{-1}, with even a clear coordination peak appearing located around at 1074.2 cm^{-1}. This indicates that the impact of coordination on the ether bond increases in the order of THP < THF < DME, which is consistent with the calculated binding energies. Although the binding energy of THF with K^+ is slightly greater than that of THP, THF has a lower coordination number with K^+ compared to THP. Due to the weak solvating capability of the solvent, the binding of potassium ions to the solvent will be weaker, which results in faster ion transport. And the solvent will be less involved in the solvating structure of potassium ion, which reduces the occurrence of solvent co-embedding phenomenon. At the same time, due to the weaker binding of the solvent to the potassium ion and less involvement of the solvent in the solvating structure, the desolvation process is easier. Taking all factors into consideration, it is assumed that THF has weaker solvating ability and would perform better with graphite anode.

We assembled the half-cells using above three kinds of electrolytes with graphite as the working electrode and potassium as the counter electrode to conduct *in-situ* X-ray diffraction (XRD) tests [29]. It verified the effect of differences in the solvation structure during potassium storage on the co-intercalation of solvent and potassium ions into graphite (Figs. 3(a)–3(c)). It can be observed that only the battery using 2 M KFSI in THP exhibits a strong peak at 32.7°, corresponding to the formation of KC_8, indicating deep potassium intercalation into the graphite. The degree of K^+ intercalation using 2 M KFSI in THF is deeper than that using 2 M KFSI in DME, but neither shows a peak for KC_8 [30], which is not consistent with the expected results. Considering that increasing the electrolyte concentration can alter the K^+ solvation structure and might prohibit the co-intercalation of solvent, we also assembled half-cells using 5 M KFSI in DME for *in-situ* XRD testing (Fig. S4 in the ESM). It presents similar results to 2 M KFSI in THP, but the peak corresponding to KC_8 is almost absent. Therefore, it is speculated that to increase the concentration of DME-based electrolyte would not favor the formation of KC_8.

Subsequently, we assembled K||graphite coin-type half-cells and conducted galvanostatic charge–discharge (GCD) tests at a current density of 0.2 C (55.8 $mA{\cdot}g^{-1}$) (Fig. 3(d)). The 2 M KFSI in DME electrolyte failed due to overcharging after only 30 cycles, with an initial specific capacity of only 229.7 $mAh{\cdot}g^{-1}$ and a remaining specific capacity of 97.4 $mAh{\cdot}g^{-1}$ after 30 cycles. Additionally, its initial Coulombic efficiency (ICE) was only 36.7%, and the CE after 30 cycles stabilized at only 97.3%. The 2 M KFSI in THF electrolyte demonstrated an ICE of 52.0% and could stably cycle for 175 cycles with a specific capacity of 193.4 $mAh{\cdot}g^{-1}$, a capacity retention rate of 95.7%, and a stabilized CE of 99.2%. The 2 M KFSI in THP electrolyte demonstrated an ICE of 49.0% and could stably cycle for 800 cycles with a specific capacity of 171.8 $mAh{\cdot}g^{-1}$, a capacity retention rate of 74.7%, and a stabilized CE of 99.3%. At 175 cycles, its specific capacity was 214.4 $mAh{\cdot}g^{-1}$ with a capacity retention rate of 93.2%. The 2 M KFSI in THP electrolyte exhibited the highest specific capacity after stable cycling and possessed an ultra-long

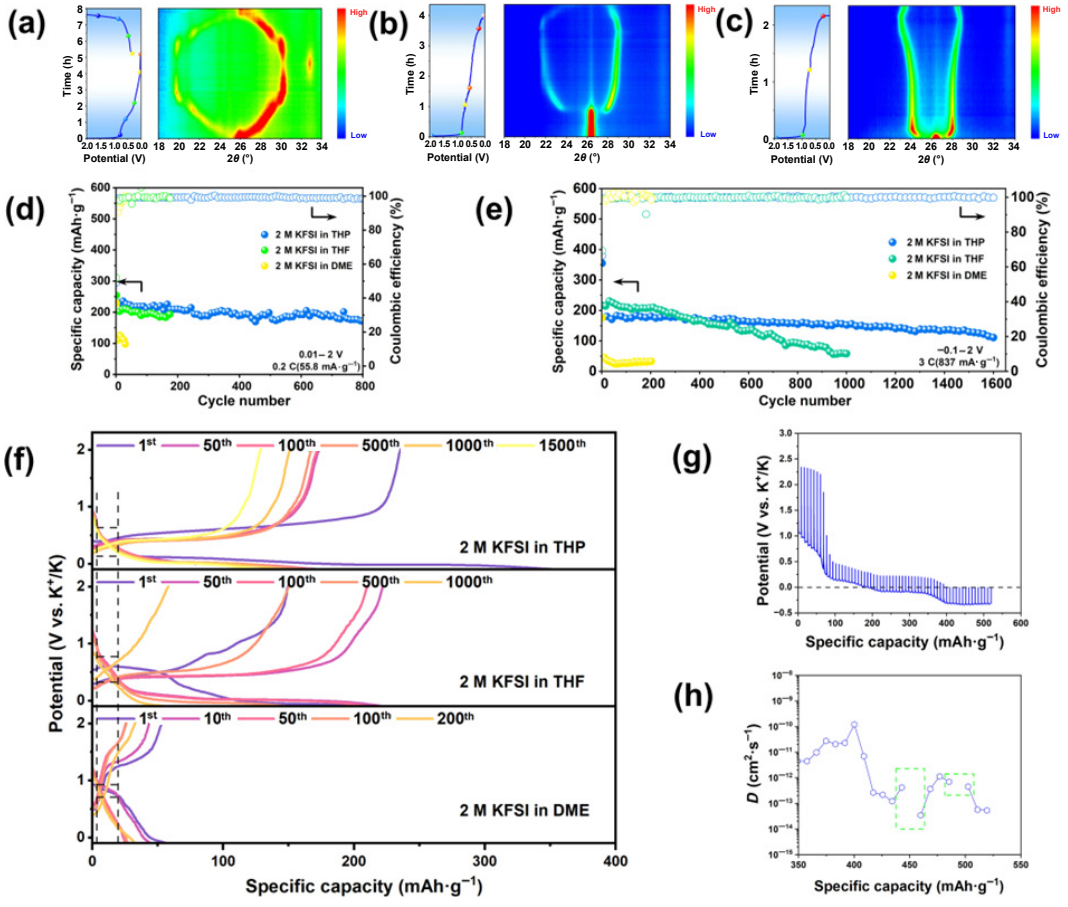

Figure 3 *In-situ* XRD of graphite with 2 M KFSI in THP (a), 2 M KFSI in THF (b), and 2 M KFSI in DME (c) electrolytes, respectively. Cycle performance at a current density of 0.2 C (d) and 3 C (e) with different electrolytes. (f) Galvanostatic charge–discharge curves of different electrolytes at a current density of 3 C. (g) GITT curve during discharge. (h) GITT-derived diffusion coefficient.

lifespan of 800 cycles. Under the high-current cycling test at 3 C (837 mA·g^{-1}) (Fig. 3(e)), the 2 M KFSI in DME electrolyte exhibited an extremely low capacity and rapidly decayed. The 2 M KFSI in THF electrolyte could stably cycle for 1000 cycles but decayed relatively quickly, with a specific capacity of only 58.1 mAh·g^{-1}. Moreover, this electrolyte displayed an activation stage of about 20 cycles, during which its capacity rose to 230.1 mAh·g^{-1} (Fig. S5 in the ESM). The 2 M KFSI in THP electrolyte could stably cycle for 1600 cycles with a specific capacity of 111.0 mAh·g^{-1} and still maintained a specific capacity of 151.4 mAh·g^{-1} at 1000th cycle. Although the capacity decayed rapidly during the first 20 cycles for this electrolyte, it still exhibited the longest cycling lifespan and the highest remaining specific capacity under high currents. The GCD curves of graphite involving in above three kinds of electrolytes at a current density of 3 C are shown in Fig. 3(f). DME exhibits a solvent co-intercalation platform at 0.9 V, and THF shows a solvent co-intercalation platform near 0.7 V, while THP does not exhibit a significant solvent co-intercalation platform (highlighted in the boxed area in Fig. 3(f)). Furthermore, during the first discharge cycle, both DME and THF exhibited obvious solvent co-intercalation platforms, while THP did not show a significant solvent co-intercalation platform even in the first cycle. Therefore, the 2 M KFSI in THP electrolyte demonstrates the best compatibility with graphite, thereby exhibiting the best electrochemical performance. During the high-current test at 3 C, due to its inherent large polarization of approximately 0.3 V (Fig. S6 in the ESM), charging and discharging at high currents would further increase the polarization. To ensure the emergence of the potassium storage platform in graphite, we adjusted the voltage to −0.1 V. Subsequently, we conducted galvanostatic intermittent titration technique (GITT) to prove its feasibility (Fig. 3(g)) [31, 32]. When discharged to 0.01 V and then left to rest, the voltage could still return to 0.4 V, indicating that potassium plating had not yet begun. The data were calculated using the Eq. (2)

$$D = \frac{4}{\pi\tau}\left(\frac{n_m V_m}{S}\right)^2\left[\frac{\Delta E_s}{\Delta E_t}\right]^2 \quad (2)$$

where τ is the relaxation time, n_m is the number of moles, V_m is the molar volume of the electrode material, S is the electrode/electrolyte contact area, ΔE_s is the voltage change caused by the pulse, ΔE_t is the voltage change during galvanostatic charging and discharging.

The diffusion coefficient of K^+ obtained from this calculation is shown in Fig. 3(h). The diffusion coefficient of K^+ drops rapidly when the specific capacity reaches 400 mAh·g^{-1}, which implied the onset of potassium deposition started from this specific capacity. Subsequently, potassium deposition begins to dominate as the specific capacity reaches 420 mAh·g^{-1}. A diffusion coefficient of 0 (highlighted in the boxed area in Fig. 3(h)) suggests that potassium deposition and dissolution have become dominant. Because the diffusion coefficient of K^+ drops rapidly when the specific capacity reaches 400 mAh·g^{-1} (corresponding to a voltage of −0.3 V), a discharge cutoff voltage of −0.1 V was set to minimize potassium deposition [33, 34]. We conducted 0.2 and 3 C galvanostatic charging and discharging tests on 5 M KFSI in DME using the same procedure (Fig. S7 in the ESM). It exhibited a higher initial capacity at 0.2 C but decayed rapidly, with only 94.2 mAh·g^{-1} remaining after 800 cycles. Besides, overcharging was observed during cycling which indicated its instability in 5 M DME system. Moreover, its 3 C performance was extremely poor, with a long activation process (about 150 cycles) and a specific capacity of only 192.4 mAh·g^{-1} after activation, which then began to decay. This indicates that while increasing the electrolyte concentration can improve electrolyte performance to some extent, it has a negative impact on cycle stability and high-current cycling performance.

To investigate the adaptability of different electrolyte with graphite anode, we conducted temperature-dependent electrochemical impedance spectroscopy (EIS) tests (Figs. 4(a)–4(c)) to compare the activation energies for the penetration of the SEI and charge transfer processes in the three kinds of electrolytes [35–37]. At 20 °C, the impedance of the three kinds of electrolytes increases in the order of THP < THF < DME, and 2 M KFSI in DME is the most affected by temperature. By taking the logarithm of the Arrhenius equation [38], we can obtain the Eq.(3)

$$\ln k = -\frac{E_a}{RT} + \ln A \quad (3)$$

where, k is the conductivity, E_a is the activation energy, R is the gas constant, and A is the pre-exponential factor.

By fitting the Randles equivalent circuit to the EIS data, we

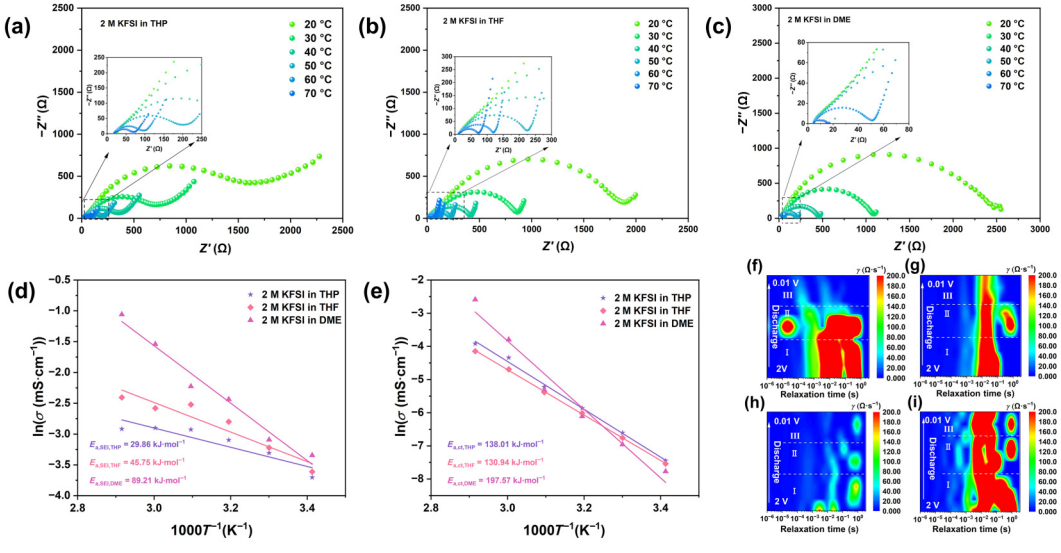

Figure 4 Temperature-dependent EIS with 2 M KFSI in THP (a), 2 M KFSI in THF (b), and 2 M KFSI in DME (c). The activation energies for different electrolytes passing through the SEI (d) and for charge transfer (e). *In situ* EIS of 2 M KFSI in THP (f), 2 M KFSI in THF (g), 2 M KFSI in DME (h), and 5 M KFSI in DME (i).

obtained the SEI impedance (R_{SEI}) and charge transfer impedance (R_{ct}). After calculating the conductivity, we plotted linear fitting curves of lnσ versus $1/T$, with the slope and intercept corresponding to the activation energy (E_a) and pre-exponential factor (A), respectively. In Fig. 4(d), the activation energies required for the three kinds of electrolytes to pass through the SEI decrease in the order of $E_{a,SEI,DME}$ (89.21 kJ·mol^{-1}) > $E_{a,SEI,THF}$ (45.75 kJ·mol^{-1}) > $E_{a,SEI,THP}$ (29.86 kJ·mol^{-1}). It can be attributed to the strong coordination between the solvent and K^+ in the electrolyte, which increases the desolvation energy barrier. This is also consistent with the DFT-calculated binding energy between K^+ and the solvent. In Fig. 4(e), the activation energies for charge transfer impedance decrease in the order of $E_{a,ct,DME}$ (197.57 kJ·mol^{-1}) > $E_{a,ct,THP}$ (138.01 kJ·mol^{-1}) > $E_{a,ct,THF}$ (130.94 kJ·mol^{-1}). By summing the activation energies for passing through the SEI and charge transfer, we obtain the total activation energy (E_a) for the interface reaction: $E_{a,THP}$ (167.87 kJ·mol^{-1}) < $E_{a,THF}$ (176.69 kJ·mol^{-1}) < $E_{a,DME}$ (286.78 kJ·mol^{-1}). Therefore, from a thermodynamic perspective, 2 M KFSI in THP has the lowest activation energy for the interface reaction, which is conducive to stable battery cycling. Subsequently, we conducted temperature-dependent EIS tests on 5 M KFSI in DME electrolyte, and the results are shown in Fig. S8 in the ESM. After increasing the concentration and reducing the coordination between K^+ and DME, the activation energy for penetrating the SEI decreased significantly (40.39 kJ·mol^{-1}), but the charge transfer activation energy increased somewhat (216.90 kJ·mol^{-1}). Overall, the total activation energy for the interface reaction decreased (257.29 kJ·mol^{-1}), which promotes stable battery cycling to a certain extent. So, the excellent thermodynamic properties of 2 M KFSI in THP result in the batteries exhibiting a longer cycle life.

In addition, we conducted *in-situ* EIS tests on the discharge processes of the four electrolytes to investigate their kinetic differences [39, 40]. The *in-situ* EIS data were processed and transformed into relaxation time distribution (DRT) data [41–45], which were plotted as two-dimensional distribution maps in Figs. 4(f)–4(i). The discharge processes of the four electrolytes are divided into three stages [46, 47]. Stage I is a rapid voltage drop stage, mainly involving ion diffusion with difficult charge transfer, where the charge transfer impedance dominates. In Stage II, the voltage drop begins to slow down, and the desolvation impedance and charge transfer impedance dominate. In Stage III, the voltage drop is the slowest as K^+ intercalates into graphite, with charge transfer impedance dominating again. Generally, Stages II and III mostly affect battery performance. In Stage II, corresponding to the impedance of K^+ ions transport the SEI, 2 M KFSI in THP exhibits significantly higher impedance compared to 2 M KFSI in THF and 2 M KFSI in DME. We attribute this increase in impedance to the desolvation process of K^+ during its transport across the SEI. Subsequently, in Stage III, due to the solvent-free co-intercalation of K^+ ions into graphite, 2 M KFSI in THP demonstrates the lowest charge transfer impedance, which is beneficial for the high-rate performance of the battery. The 5 M KFSI in DME electrolyte has high charge transfer impedance throughout the discharge process due to its increased concentration, affecting its cycle stability and life. Therefore, the superior kinetic characteristics exhibited by 2 M KFSI in THP ensure stable cycling of the batteries at a high current density of 3 C (837 mA·g^{-1}).

Subsequently, we conducted X-ray photoelectron spectroscopy (XPS) etching characterization on the graphite electrodes after five cycles at a current density of 0.2 C with three types of electrolytes to investigate the composition of the resulted SEI. The S 2p spectra involving the electrolyte of 2 M KFSI in THP, 2 M KFSI in THF, and 2 M KFSI in DME are presented in Figs. 5(a)–5(c). S originates from the decomposition of anions in KFSI, with a binding energy of 168.5 eV corresponding to the O=S=O group. In the SEI formed by 2 M KFSI in THP, the substantial decrease in the proportion of O=S=O after 30 s of etching indicates that most of the S in the SEI exists in an inorganic form. In contrast, for the formed SEI induced by 2 M KFSI in THF, the slow decrease in the proportion of O=S=O with increasing etching time suggests that S in its SEI primarily exists in an organic form, with a higher content of organic components nearer the surface. For the SEI formed by 2 M KFSI in DME, the almost unchanged proportion of O=S=O with increasing etching time indicates that most of the S in its SEI exists in an organic form. The C 1s spectrum, shown in Fig. S9 in the ESM, exhibits a distinct peak for C–O only in 2 M KFSI in THF, indicating THF involves the decomposition in the formation of the SEI. Therefore, the SEI induced by 2 M KFSI in THP is predominantly composed of inorganic components, making it thin, robust, and conducive to ion transport [48, 49]. Moreover, the S 2p and C 1s spectra related to 5 M KFSI in DME electrolyte are presented in Fig. S10 in the ESM. It can be seen that increasing the concentration of the electrolyte can enhance the decomposition degree of FSI^- and increase the content of inorganic components in SEI. Subsequently, transmission electron microscopy (TEM) and scanning electron microscopy (SEM) images of the electrodes after five cycles with the four electrolytes are collected. The obtained TEM images are shown in Figs. 5(d)–5(g). It can be seen that the SEI produced by 2 M KFSI in THP is the thinnest and most uniform, with a thickness of only about 5.9 nm. The SEI produced by 2 M KFSI in THF is also relatively uniform, with a thickness of about 10.8 nm. The SEI produced by 2 M KFSI in DME is up to 38.9 nm thick and very uneven, with some areas exceeding 50 nm in thickness. The SEI produced by 5 M KFSI in DME is about 10.9 nm thick but also not very uniform. The corresponding mapping images shown in Fig. S11 in the ESM indicate that the main components of the SEI are the elements tested in the aforementioned XPS analysis. In Figs. 5(h)–5(k), it can be observed that only the graphite electrode using 2 M KFSI in THP electrolyte maintains good morphology after cycling, while the other three electrolytes result in varying degrees of damage to the graphite after cycling. This is also one of the reasons why the 2 M KFSI in THP electrolyte enables the graphite anode to exhibit a long lifespan for potassium ion batteries.

Finally, the full cell was assembled with PTCDI as positive electrode and graphite as negative electrode with each of the three kinds of electrolytes (Fig. S12 (a) in the ESM). At a current density of 100 mA·g^{-1}, the THP-based electrolyte showed the best cycling performance and stable CE, the THF-based electrolyte displayed unstable CE and poor cycling performance, and the DME-based electrolyte exhibited greater than 120% CE in cycling and very poor cycling performance. In addition, the corresponding galvanostatic charge–discharge curves of the three kinds of electrolytes (Figs. S12(b)–S12(d) in the ESM) have a clear plateau only for the THP-based electrolyte. Therefore, THP-based electrolyte has the best compatibility in the full battery.

3 Conclusions

In summary, this work demonstrated a weakly solvating cyclic ether electrolyte with THP as the solvent, which was first used for the

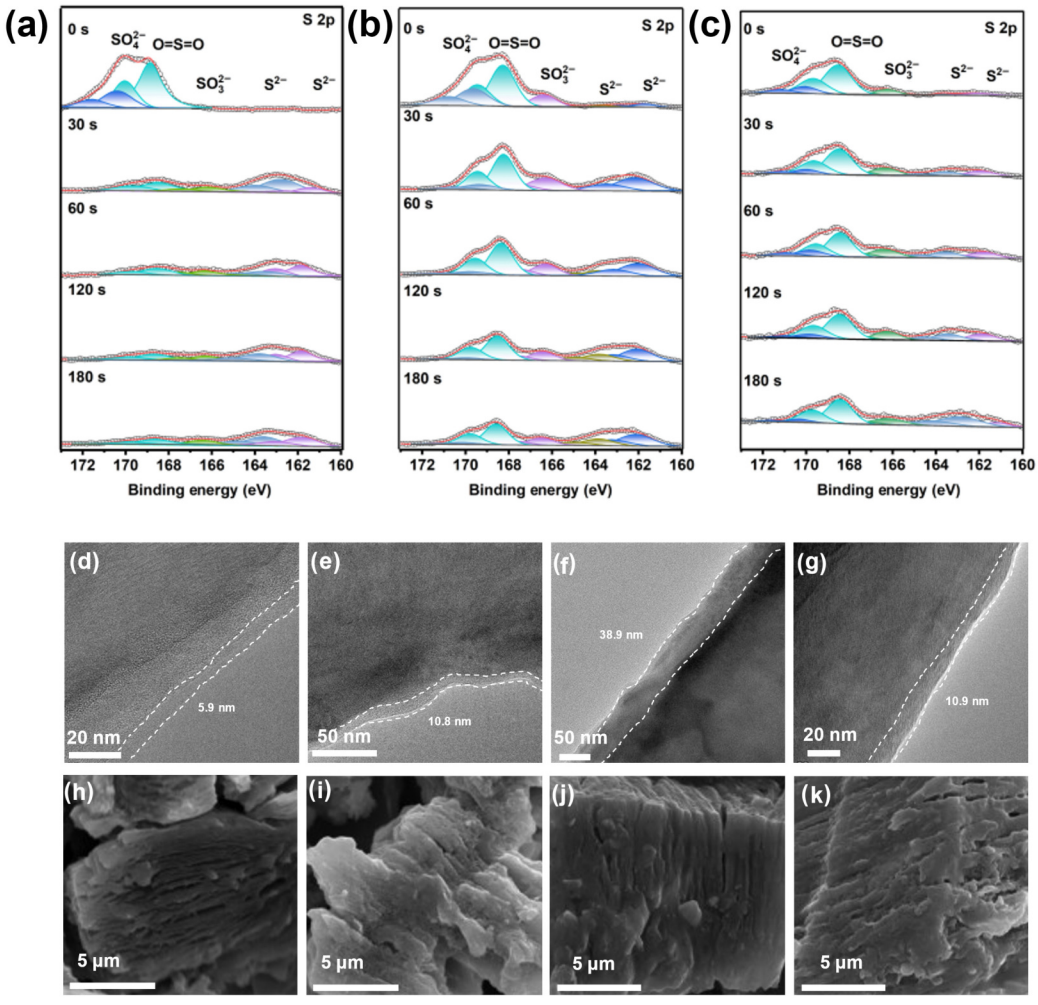

Figure 5 The XPS spectra of S 2p for 2 M KFSI in THP (a), 2 M KFSI in THF (b), and 2 M KFSI in DME (c). TEM images of graphite with 2 M KFSI in THP (d), 2 M KFSI in THF (e), 2 M KFSI in DME (f), and 5 M KFSI in DME (g). SEM images of graphite with 2 M KFSI in THP (h), 2 M KFSI in THF (i), 2 M KFSI in DME (j), and 5 M KFSI in DME (k).

graphite anode of potassium-ion batteries. In this electrolyte, the steric hindrance imparted by the cyclic structure of THP weakens its coordination with K^+, thereby increasing the coordination between K^+ and anions. This promotes the decomposition of more FSI^- during the formation of the SEI, leading to the formation of a thin and dense SEI rich in inorganic components. The low binding energy between K^+ and THP facilitates rapid desolvation, making electrode interface reactions more thermodynamically favorable. Thus, the use of this THP-based electrolyte allows for stable cycling at a current density of 0.2 C for 800 cycles (approximately 8 months) with a specific capacity of 171.8 mAh·g^{-1}, and stable cycling at a current density of 3 C for 1600 cycles with a specific capacity of 111.0 mAh·g^{-1}. These findings provide a new type of electrolyte for potassium-ion batteries, potentially inspiring further advancements for next-generation potassium-ion batteries and beyond.

Electronic Supplementary Material: Supplementary material (materials and methods; electrochemical characterization; MD simulations; DFT simulations; LSV; IR; *in situ* XRD image; EIS; XPS; TEM mapping; full cell performance comparison) is available in the online version of this article at https://doi.org/10.26599/NR.2025.94907219.

Data availability

All data needed to support the conclusions in the paper are presented in the manuscript and the Electronic Supplementary Material. Additional data related to this paper may be requested from the corresponding author upon request.

Acknowledgements

The authors greatly appreciate the financial support from the National Key Research and Development Program of China (No. 2022YFB2404300) and the National Natural Science Foundation of China (Nos. 22409153 and 52101269).

Declaration of competing interest

All the contributing authors report no conflict of interests in this work.

Author contribution statement

C. J. C.: Data curation (Lead), formal analysis (Lead), investigation (Equal), methodology (Equal), writing – original draft (Lead). W. C. F.: Data curation (Equal), formal analysis (Equal), investigation

(Equal), methodology (Equal), validation (Equal). F. Y. W.: Data curation (Supporting), formal analysis (Supporting), investigation (Equal), methodology (Equal). J. K. R.: Conceptualization (Equal), investigation (Equal), methodology (Equal). D. Y. G.: Investigation (Equal), methodology (Equal), project administration (Lead), validation (Equal). W. C.: Conceptualization (Equal), project administration (Equal), supervision (Equal). J.-J. G.: Supervision (Supporting). K. F.: Funding acquisition (Supporting), supervision (Supporting). X. B. L.: Formal analysis (Equal), funding acquisition (Supporting), supervision (Equal), visualization (Lead). W. L.: Funding acquisition (Lead), investigation (Equal), supervision (Lead), writing – review & editing (Lead).

Use of AI statement

None.

References

[1] Gür, T. M. Review of electrical energy storage technologies, materials and systems: Challenges and prospects for large-scale grid storage. *Energy Environ. Sci.* **2018**, *11*, 2696–2767.

[2] Eftekhari, A.; Jian, Z. L.; Ji, X. L. Potassium secondary batteries. *ACS Appl. Mater. Interfaces* **2017**, *9*, 4404–4419.

[3] Fan, L.; Ma, R. F.; Zhang, Q. F.; Jia, X. X.; Lu, B. G. Graphite anode for a potassium-ion battery with unprecedented performance. *Angew. Chem., Int. Ed.* **2019**, *58*, 10500–10505.

[4] Zheng, J.; Yang, Y.; Fan, X. L.; Ji, G. B.; Ji, X.; Wang, H. Y.; Hou, S.; Zachariah, M. R.; Wang, C. S. Extremely stable antimony-carbon composite anodes for potassium-ion batteries. *Energy Environ. Sci.* **2019**, *12*, 615–623.

[5] Wang, L.; Zhang, B.; Wang, B.; Zeng, S. Y.; Zhao, M. W.; Sun, X. P.; Zhai, Y. J.; Xu, L. Q. *In-situ* nano-crystallization and solvation modulation to promote highly stable anode involving alloy/de-alloy for potassium ion batteries. *Angew. Chem., Int. Ed.* **2021**, *60*, 15381–15389.

[6] Xu, F.; Zhai, Y. X.; Zhang, E.; Liu, Q. H.; Jiang, G. S.; Xu, X. S.; Qiu, Y. Q.; Liu, X. M.; Wang, H. Q.; Kaskel, S. Ultrastable surface-dominated pseudocapacitive potassium storage enabled by edge-enriched N-doped porous carbon nanosheets. *Angew. Chem., Int. Ed.* **2020**, *59*, 19460–19467.

[7] Wu, X. Y.; Leonard, D. P.; Ji, X. L. Emerging non-aqueous potassium-ion batteries: Challenges and opportunities. *Chem. Mater.* **2017**, *29*, 5031–5042.

[8] Jian, Z. L.; Luo, W.; Ji, X. L. Carbon electrodes for K-ion batteries. *J. Am. Chem. Soc.* **2015**, *137*, 11566–11569.

[9] Wang, Z. H.; Selbach, S. M.; Grande, T. Van der Waals density functional study of the energetics of alkali metal intercalation in graphite. *RSC Adv.* **2014**, *4*, 4069–4079.

[10] Wu, X. F.; Li, Z. J.; Liu, J. X.; Luo, W.; Gaumet, J. J.; Mai, L. Q. Defect engineering of hierarchical porous carbon microspheres for potassium-ion storage. *Rare Met.* **2022**, *41*, 3446–3455.

[11] Wu, X.; Chen, Y. L.; Xing, Z.; Lam, C. W. K.; Pang, S. S.; Zhang, W.; Ju, Z. C. Advanced carbon-based anodes for potassium-ion batteries. *Adv. Energy Mater.* **2019**, *9*, 1900343.

[12] Liu, Q.; Fan, L.; Chen, S. H.; Su, S. L.; Ma, R. F.; Han, X.; Lu, B. Antimony-graphite composites for a high-performance potassium-ion battery. *Energy Technol.* **2019**, *7*, 1900634.

[13] Feng, W. C.; Pan, C. Q.; Wang, H.; Zhang, B. L.; Luo, W.; Shen, C. L.; Wang, J. J.; Cheng, C. J.; Xv, X. M.; Yu, R. H. et al. Molecular carbon skeleton with self-regulating ion-transport channels for long-life potassium ion batteries. *Energy Storage Mater.* **2023**, *63*, 102975.

[14] Wang, F. Y.; Yang, T.; Feng, W. C.; Ren, J. K.; Chen, X. B.; Cheng, C. J.; Luo, W.; Liao, X. B.; Mai, L. Q. Homogeneous adsorption of multiple potassiation products of red phosphorus anode toward stable potassium storage. *ACS Nano* **2024**, *18*, 17197–17208.

[15] Feng, W. C.; Wang, H.; Jiang, Y. L.; Zhang, H. Z.; Luo, W.; Chen, W.; Shen, C. L.; Wang, C. X.; Wu, J. S.; Mai, L. Q. A strain-relaxation red phosphorus freestanding anode for non-aqueous potassium ion batteries. *Adv. Energy Mater.* **2022**, *12*, 2103343.

[16] Zhang, Q.; Mao, J. F.; Pang, W. K.; Zheng, T.; Sencadas, V.; Chen, Y. Z.; Liu, Y. J.; Guo, Z. P. Boosting the potassium storage performance of alloy-based anode materials via electrolyte salt chemistry. *Adv. Energy Mater.* **2018**, *8*, 1703288.

[17] Li, T.; Wang, Y. K.; Zhou, Q. W.; Yuan, L. L.; Qiao, S. Y.; Ma, M.; Liu, Z. Q.; Chong, S. K. SnTe nanoparticles physicochemically encapsulated by double carbon as conversion-alloying anode materials for superior potassium-ion batteries. *J. Mater. Sci. Technol.* **2023**, *158*, 86–95.

[18] Wen, S.; Gu, X.; Ding, X. W.; Dai, P. C.; Zhang, D. J.; Li, L. J.; Liu, D. D.; Zhao, X. B.; Yang, J. Boosting fast and stable alkali metal ion storage by synergistic engineering of oxygen vacancy and amorphous structure. *Adv. Funct. Mater.* **2022**, *32*, 2106751.

[19] Wen, S.; Gu, X.; Ding, X. W.; Zhang, L.; Dai, P. C.; Li, L. J.; Liu, D. D.; Zhang, W. C.; Zhao, X. B.; Guo, Z. P. Constructing ultrastable electrode/electrolyte interface for rapid potassium ion storage capability via salt chemistry and interfacial engineering. *Nano Res.* **2022**, *15*, 2083–2091.

[20] Sun, Z. N.; Liang, H. Y.; Wang, H. L.; Shi, J.; Huang, M. H.; Chen, J. W.; Liu, S.; Tian, W. Q.; Cao, H. J.; Li, Z. Spatially confined "edge-to-edge" strategy for achieving compact Na^+/K^+ storage: Constructing hetero-Ni/Ni_3S_2 in densified carbons. *Adv. Funct. Mater.* **2022**, *32*, 2203291.

[21] Luo, W. D.; Feng, Y. H.; Shen, D. Y.; Zhou, J.; Gao, C. T.; Lu, B. G. Engineering ion diffusion by CoS@SnS heterojunction for ultrahigh-rate and stable potassium batteries. *ACS Appl. Mater. Interfaces* **2022**, *14*, 16379–16385.

[22] Li, T.; Zhang, Q. Advanced metal sulfide anode for potassium ion batteries. *J. Energy Chem.* **2018**, *27*, 373–374.

[23] Zhang, B.; Xu, B. H.; Qin, H. Z.; Cao, L.; Ou, X. Highly active and stable Cu_9S_5-MoS_2 heterostructures nanocages enabled by dual-functional Cu electrocatalyst with enhanced potassium storage. *J. Mater. Sci. Technol.* **2023**, *143*, 107–116.

[24] Zhou, M. F.; Bai, P. X.; Ji, X.; Yang, J. X.; Wang, C. S.; Xu, Y. H. Electrolytes and interphases in potassium ion batteries. *Adv. Mater.* **2021**, *33*, 2003741.

[25] Wang, L. P.; Yang, J. Y.; Li, J.; Chen, T.; Chen, S. L.; Wu, Z. R.; Qiu, J. L.; Wang, B. J.; Gao, P.; Niu, X. B. et al. Graphite as a potassium ion battery anode in carbonate-based electrolyte and ether-based electrolyte. *J. Power Sources* **2019**, *409*, 24–30.

[26] Zhang, J. M.; Li, Q. P.; Zeng, Y. P.; Tang, Z.; Sun, D.; Huang, D.; Peng, Z. G.; Tang, Y. G.; Wang, H. Y. Non-flammable ultralow concentration mixed ether electrolyte for advanced lithium metal batteries. *Energy Storage Mater.* **2022**, *51*, 660–670.

[27] Liao, Y. Q.; Zhou, M. Y.; Yuan, L. X.; Huang, K.; Wang, D. H.; Han, Y.; Meng, J. T.; Zhang, Y.; Li, Z.; Huang, Y. H. Eco-friendly tetrahydropyran enables weakly solvating "4S" electrolytes for lithium-metal batteries. *Adv. Energy Mater.* **2023**, *13*, 2301477.

[28] Hu, X. X.; Zheng, H. P.; Tao, R.; Wang, P. Migration of nitrite corrosion inhibitor in calcium silicate hydrate nanopore: A molecular dynamics simulation study. *Front. Mater.* **2022**, *9*, 965772.

[29] Li, Q.; Zhang, Y. B.; Chen, Z. Y.; Zhang, J.; Tao, Y.; Yang, Q. H. Discrete graphitic crystallites promise high-rate ion intercalation for KC_8 formation in potassium ion batteries. *Adv. Energy Mater.* **2022**, *12*, 2201574.

[30] Liang, L.; Tang, M. Y.; Zhu, Q. N.; Wei, W.; Wang, S. C.; Wang, J. W.; Chen, J. C.; Yu, D. D.; Wang, H. Chemical prepotassiation realizes scalable KC_8 foil anodes for potassium-ion pouch cells. *Adv. Energy Mater.* **2023**, *13*, 2300453.

[31] Liu, K.; Gao, Y. F.; Fang, Z. Y.; Zhou, X. Y.; Ma, Y.; Wu, H. Y.;

Kang, M. L.; Wang, B. Determination of diffusion coefficients of uranium in liquid gallium by GITT. *J. Electroanal. Chem.* **2020**, *879*, 114711.
[32] Heubner, C.; Schneider, M.; Michaelis, A. SoC dependent kinetic parameters of insertion electrodes from staircase-GITT. *J. Electroanal. Chem.* **2016**, *767*, 18–23.
[33] Jiang, H. Z.; Yang, C.; Chen, M.; Liu, X. W.; Yin, L. M.; You, Y.; Lu, J. Electrophilically trapping water for preventing polymerization of cyclic ether towards low-temperature li metal battery. *Angew. Chem., Int. Ed.* **2023**, *62*, e202300238.
[34] Cheng, L. W.; Lan, H.; Gao, Y.; Dong, S.; Wang, Y. Y.; Tang, M. Y.; Sun, X. Y.; Huang, W. R.; Wang, H. Realizing low-temperature graphite-based rechargeable potassium-ion full battery. *Angew. Chem.* **2024**, *136*, e202315624.
[35] Yaghoobnejad Asl, H.; Stanley, P.; Ghosh, K.; Choudhury, A. Iron borophosphate as a potential cathode for lithium- and sodium-ion batteries. *Chem. Mater.* **2015**, *27*, 7058–7069.
[36] Zabara, M. A.; Katırcı, G.; Ülgüt, B. *Operando* investigations of the interfacial electrochemical kinetics of metallic lithium anodes via temperature-dependent electrochemical impedance spectroscopy. *J. Phys. Chem. C* **2022**, *126*, 10968–10976.
[37] Weng, S. T.; Zhang, X.; Yang, G. J.; Zhang, S. M.; Ma, B. Y.; Liu, Q. Y.; Liu, Y.; Peng, C. X.; Chen, H. X.; Yu, H. L. et al. Temperature-dependent interphase formation and Li^+ transport in lithium metal batteries. *Nat. Commun.* **2023**, *14*, 4474.
[38] Li, X. Y.; Feng, S.; Song, Y. W.; Zhao, C. X.; Li, Z.; Chen, Z. X.; Cheng, Q.; Chen, X.; Zhang, X. Q.; Li, B. Q. et al. Kinetic evaluation on lithium polysulfide in weakly solvating electrolyte toward practical lithium-sulfur batteries. *J. Am. Chem. Soc.* **2024**, *146*, 14754–14764.
[39] Qiu, D. P.; Zhao, W. T.; Zhang, B.; Ahsan, M. T.; Wang, Y. H.; Zhang, L. L.; Yang, X. L.; Hou, Y. L. Ni-single atoms modification enabled kinetics enhanced and ultra-stable hard carbon anode for sodium-ion batteries. *Adv. Energy Mater.* **2024**, *14*, 2400002.
[40] Kitz, P. G.; Lacey, M. J.; Novák, P.; Berg, E. J. *Operando* EQCM-D with simultaneous *in situ* EIS: New insights into interphase formation in Li ion batteries. *Anal. Chem.* **2019**, *91*, 2296–2303.
[41] Lu, Y.; Zhao, C. Z.; Huang, J. Q.; Zhang, Q. The timescale identification decoupling complicated kinetic processes in lithium batteries. *Joule* **2022**, *6*, 1172–1198.
[42] Wan, T. H.; Saccoccio, M.; Chen, C.; Ciucci, F. Influence of the discretization methods on the distribution of relaxation times deconvolution: Implementing radial basis functions with DRTtools. *Electrochim. Acta* **2015**, *184*, 483–499.
[43] Weiß, A.; Schindler, S.; Galbiati, S.; Danzer, M. A.; Zeis, R. Distribution of relaxation times analysis of high-temperature PEM fuel cell impedance spectra. *Electrochim. Acta* **2017**, *230*, 391–398.
[44] Chen, J.; Quattrocchi, E.; Ciucci, F.; Chen, Y. H. Charging processes in lithium-oxygen batteries unraveled through the lens of the distribution of relaxation times. *Chem* **2023**, *9*, 2267–2281.
[45] Schönleber, M.; Klotz, D.; Ivers-Tiffée, E. A method for improving the robustness of linear kramers-kronig validity tests. *Electrochim. Acta* **2014**, *131*, 20–27.
[46] Zhang, W. L.; Ming, J.; Zhao, W. L.; Dong, X. C.; Hedhili, M. N.; Costa, P. M. F. J.; Alshareef, H. N. Graphitic nanocarbon with engineered defects for high-performance potassium-ion battery anodes. *Adv. Funct. Mater.* **2019**, *29*, 1903641.
[47] Cao, B.; Zhang, Q.; Liu, H.; Xu, B.; Zhang, S. L.; Zhou, T. F.; Mao, J. F.; Pang, W. K.; Guo, Z. P.; Li, A. et al. Graphitic carbon nanocage as a stable and high power anode for potassium-ion batteries. *Adv. Energy Mater.* **2018**, *8*, 1801149.
[48] Zvereva, E.; Caliste, D.; Pochet, P. Interface identification of the solid electrolyte interphase on graphite. *Carbon* **2017**, *111*, 789–795.
[49] Chen, Y. Y.; Huang, H. Y.; Liu, L. L.; Chen, Y. X.; Han, Y. S. Diffusion enhancement to stabilize solid electrolyte interphase. *Adv. Energy Mater.* **2021**, *11*, 2101774.